Check for updates

Received: 17 July 2025 | Revised: 10 February 2026 | Accepted: 24 February 2026

DOI: 10.1002/aic.70336

AIChE JOURNAL

RESEARCH ARTICLE

Particle Technology and Fluidization

Erosion of granular sediments by submerged impinging jets: Particle size effects and cohesion onset

Ahmad Mohamadiyeh[1,2] | Jeffrey Peakall[3] | Michael Fairweather[2] | Martyn Barnes[4] | Timothy N. Hunter[2]

[1]Center for Doctoral Training (CDT) in Future Fluid Dynamics, University of Leeds, Leeds, UK

[2]School of Chemical and Process Engineering, University of Leeds, Leeds, UK

[3]School of Earth and Environment, University of Leeds, Leeds, UK

[4]Sellafield Ltd, Warrington, UK

Correspondence
Ahmad Mohamadiyeh, Center for Doctoral Training (CDT) in Future Fluid Dynamics, University of Leeds, Leeds, LS2 9JT, UK.
Email: scamm@leeds.ac.uk

Funding information
EPSRC Centre of Doctoral Training in Fluid Dynamics at Leeds, Grant/Award Number: EP/S022732/1; EPSRC MULTIForm National Nuclear Users Facility, Grant/Award Number: EP/V034898/1

Abstract

This study investigates the erosion behavior and modeling of glass particle beds under impinging jet conditions, with a focus on particle size effects and the onset of cohesion. Ultrasonic profiling is implemented to scan and measure static crater profiles. Results indicate that particle size significantly affects crater dimensions, ring peak formation, and overall crater shape. The smallest glass particles ($d_{50} = 35$ μm) studied deviate from the trends in crater size, yield stress, and analytical modeling established using larger particles, indicating the onset of cohesion effects at this small particle size. The standard erosion parameter worked well for modeling cohesionless particles down to a certain size limit, beyond which cohesive forces become significant. A new parameter, E_τ based on particle critical shear stress, is introduced for erosion modeling in this study. The transition to cohesive behavior observed in the smallest glass particles is successfully accounted for using E_τ.

KEYWORDS
erosion, glass beads, impinging jets, LiDAR, ultrasonic velocity profiler

1 | INTRODUCTION

The erosion of sediment beds by turbulent impinging jets is of considerable interest due to its relevance in a wide range of applications. For example, impinging jets are used in cleaning operations to erode and remove debris and silt,[1] for measuring the erodibility of soils and the shear strength of sediment beds,[2,3] and for landing rockets on planetary surfaces.[4] One of the most relevant applications for this investigation is nuclear waste management. Submerged liquid impinging jets are employed across many nuclear sites, especially in the United States and the United Kingdom, to mix and erode consolidated nuclear waste remotely.[5–7] Impinging jets are preferred to conventional mechanical mixers given the harsh radioactive environment created by nuclear waste. Specifically, impinging jets are implemented at Sellafield in the United Kingdom within the Highly Active Storage Tanks (HASTs) to disperse precipitated nuclear waste. The nuclear waste within the HASTs consists of nitric acid and a host of nuclear fission products from Highly Active Liquor (HAL) wastes arising from nuclear reprocessing.[8,9] Impinging jets are used to erode settled particles and keep them in mobile suspension, preventing the formation of highly durable sediment beds and radioactive hotspots.

Further understanding of the fundamentals of erosion by impinging jets is crucial, especially for nuclear waste management facilities where direct measurements and monitoring are difficult given the hazardous radioactive environment.[7] Therefore, it is required to investigate experimentally impinging jet erosion on non-radioactive simulants. In addition to the properties of the fluid and the jet itself, the properties of the sediment bed particles play a significant role in the

This is an open access article under the terms of the Creative Commons Attribution License, which permits use, distribution and reproduction in any medium, provided the original work is properly cited.
© 2026 The Author(s). *AIChE Journal* published by Wiley Periodicals LLC on behalf of American Institute of Chemical Engineers.

erosion. The focus of this study is on sediments composed of spherical glass beads with different particle sizes and distributions, which exhibit a transition from cohesionless to cohesive as they get smaller (and their surface area to volume ratio proportionally increases). This transition is commonly attributed to the increasing importance of interparticle cohesive forces (e.g., van der Waals and electrostatic interactions) relative to particle weight as particle size decreases. Previous studies have shown that this shift becomes relevant in the fine-sediment regime, typically around 100 μm.[10–13]

In a typical submerged impinging jet, the flow can be described in terms of three distinct regions: the free-jet region, the impingement region, and the wall-jet region.[14] In the free-jet region, the jet develops and spreads while mixing with the surrounding fluid. As the jet evolves, entrainment increases and the jet boundary grows.[15] As the jet approaches the bed surface, it enters the impingement region, where the axial velocity decreases sharply and the static pressure rises.[14] The axial momentum is then redirected into a radial outflow that forms a near-bed wall jet. As erosion progresses, the evolving bed topography can in turn modify the impingement and wall-jet flow regions.

For cohesionless beds, erosion is governed by the balance of the shear stress exerted by the fluid jet on the particles and the gravity force acting on them. The particles erode individually based on this force balance, with minimal inter-particle cohesion. Aderibigbe and Rajaratnam[16] studied the erosion of cohesionless sand beds by submerged circular impinging jets, using the dimensionless critical erosion parameter, $E_c = (UD/h)/\sqrt{(gd(\rho_s - \rho_f)/\rho_f)}$, to model their erosion, where g is gravity and ρ_f is fluid density. E_c accounts for both jet-related variables, such as nozzle diameter (D), exit velocity (U), and jet height (h), and macroscopic particle properties, including particle size (d) and density (ρ_s). The authors categorized the flow into two regimes based on E_c: Strongly Deflected Jet Regime and Weakly Deflected Jet Regime, and derived scale-independent relationships for scour depth and length. Subsequently, this approach has been frequently used in cohesionless impinging jet erosion studies.[17–19] For instance, in a recent study, Chen et al.[19] proposed a power-law relationship for dynamic scour depth by recalibrating E_c using their experimental data.

In contrast, modeling erosion in cohesive beds is more challenging, as cohesive forces become dominant over gravitational forces, limiting the relevance and accuracy of using E_c in cohesive sediments.[20] To address this, alternative modeling approaches have been explored in the literature to account for the resisting stresses within cohesive beds. Hamm et al.[21] predicted the cleaning radius using wall jets in nuclear waste applications by considering a force balance between the jet and the resisting stress within the bed. Moreover, Mazurek et al.[22] estimated crater dimensions using parameters derived from dimensional analysis, incorporating the critical shear stress of the bed and the shear stress applied by the fluid. More recently, Brunier-Coulin et al.[23] proposed a generalized form of the Shields criterion based on a cohesion number derived from tensile yield strength measurements. They induced cohesion using both liquid capillary bridges and solid resin bonds and quantified the resulting cohesive strength through dedicated tensile tests. Their results show that the proposed formulation reconciles experimental data for both cohesionless and cohesive granular materials.

Several papers have investigated the erosion of cohesionless sediment beds by submerged liquid impinging jets.[17,18,24–28] These studies examined the shapes of the scours and their temporal evolution, as well as the effects of jet properties, such as jet velocity, shape, and height, on scour size. Nevertheless, relatively few studies have focused on the direct influence of the macroscopic physical properties of cohesionless beds on erosion. Of note, Guleria and Patil[29] studied the effect of particle size on impinging jet erosion, using relatively large glass beads (diameter, $d = 1–7$ mm). They found that particle polydispersity influences the crater shape, and that the growth rate of the crater depends on particle size. Similarly, LaMarche and Curtis[30] investigated the influence of particle shape, density, and size ($d = 0.046–2.3$ mm) on crater growth. With respect to particle size, they observed that larger particles lead to a faster initial growth rate, whereas smaller particles result in faster crater growth at later times. Notably, both studies implemented air impinging jets. Although there are similarities between submerged liquid jets and air jets, the erosive mechanisms and resulting scour patterns can differ. In addition to the typical scour Form I (shallow parabolic craters) and scour Form II (deep conical craters) observed in submerged liquid jets.[16,19] Additional shapes featuring an inner curve and outer straight parts have been reported in air jets.[29,31]

The aim of this investigation is to study the effects of particle size on erosion by submerged liquid jets and determine the limits of particle size on analytical modeling. To achieve this, soda lime glass beads with different size distributions and median diameters ranging from 35 to 543 μm were used. In previous studies, glass beads have been considered as cohesionless particles due to their sphericity and relatively large size.[29,30] Interestingly, in this study, we test a wider range of particle sizes, allowing us to validate the behavior of the larger particles and explore whether smaller particles start to exhibit any cohesion effects. This comprehensive size range covers most of the particle sizes that may be present in the HASTs, providing a thorough investigation of the effects of size on erosion by impinging jets.[7,32] A central question addressed is whether the critical erosion parameter, E_c, remains a reliable scaling parameter for correlating erosion behavior across the full particle size range, particularly for smaller particles where interparticle forces may become increasingly significant. In addition, this study proposes an alternative erosion parameter, E_τ, based on shear yield-stress measurements, which has not previously been applied to erosion of cohesionless sediments by impinging jets and offers a potentially more comprehensive representation of erosion processes.

2 | MATERIALS AND METHODS

2.1 | Materials

The particles used were soda-lime spherical glass particles, known commercially as "Honite" (Guyson Ltd., UK). K.Chemically, the

15475905, 2026, 6, Downloaded from https://aiche.onlinelibrary.wiley.com/doi/10.1002/aic.70336 by University Of Leeds The Brotherton Library, Wiley Online Library on [28/05/2026]. See the Terms and Conditions (https://onlinelibrary.wiley.com/terms-and-conditions) on Wiley Online Library for rules of use; OA articles are governed by the applicable Creative Commons License

particles consist of SiO_2 (75%), Na_2O (15%), CaO (10%), and MgO (5%) with a density of approximately 2500 kg/m^3.[33] HX is the used abbreviation for the Honite particles, where H refers to "Honite" and "X" indicates the particle grade. The larger the value of X, the smaller the size distribution of Honite particles. Five different Honite grades were studied in this work: H8, H9, H12, H16 and H22.

2.2 | Particle size and morphology

The particle size distributions (PSDs) of the particles were found using laser diffraction characterization, with a Mastersizer 3000 (Malvern Panalytical Ltd., UK). K.Five measurement runs were conducted per sample per particle type and then the PSDs were averaged. The variations between the five measurements in each case were minimal (<3%). Figure 1 shows the resulting mean size distributions of all five Honite grades used.

The Honite size distributions were fitted to log-normal distributions, where the mean size of the particles (d_{mean}) and the standard deviation (SD) were found. This allowed the coefficient of variation (CV) to be calculated according to CV = SD/d_{mean}, with this coefficient being a useful way to quantify the variation of the distribution.[34] Table 1 summarizes the median (d_{50}), 10th percentile (d_{10}), and 90th percentile (d_{90}) particle sizes obtained from the Mastersizer, as well as the coefficient of variation, CV (%), obtained from the log-normal fits. The coefficients of variation of H8, H9, H12, and H16 were all relatively small, while the smallest size, H22, was slightly more polydisperse than the other particle types, likely because these represented the smallest sieve size fractions. Nevertheless, the CVs were all small enough that it was assumed erosion behavior could be modeled through their median (d_{50}) sizes alone.[35,36]

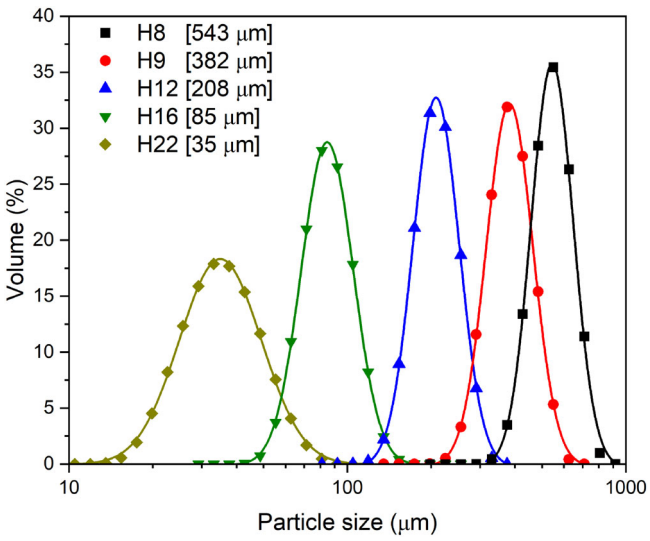

FIGURE 1 Measured mean particle size distributions (PSDs) of Honite glass particles. Honite grade [median size: d_{50}]. The continuous lines represent fitted log-normal distributions.

A TM3030Plus scanning electron microscope ("SEM," Hitachi-high tech, Japan) was used to assess the morphology of the glass particles. As shown in Figure 2, all the particle grades (H22, H16, H12, H9 and H8) were generally spherical, while there were a few outliers in each fraction that had slightly irregular shapes. This may be due to external mechanical stress acting on the particles during handling, transportation and processing, or simply from their synthesis in manufacture. In addition, Figure 2 confirms the results of the Mastersizer that show that H22 had higher variations in size than the other glass particles and was less well sorted.

2.3 | Yield shear stress measurements

A vane viscometer, DV2T-extra (Brookfield Ltd., USA), was used to measure the yield stress of the five different Honite particles to determine their strength. A four-bladed vane was attached to the viscometer and then immersed in a sample. The four-bladed vane rotates slowly at a constant rate in the sample to detect the yielding moment, when the torque exerted on the vane reaches a maximum. The maximum torque (T_{max}) is related to the yield stress (τ) by the following equation[37]:

$$T_{max} = \frac{\pi D_{vane}^3}{2}\left(\frac{H}{D} + \frac{1}{6}\right)\tau, \quad (1)$$

where D_{vane} is the diameter of the vane and H is its effective length. The "V-74" vane (D_{vane} = 0.589 cm and H = 1.176 cm) was used in all experiments. Suspensions were prepared in a 100 mL beaker that was large compared to the vane to avoid any wall effects (D_{beaker}/D_{vane} >2).[38] The suspensions were prepared at a volume fraction of ~60 vol % and left to settle for 5 min. This volume fraction is representative of the packing fraction of loose-packed beds of spherical particles.[39] The vane was then submerged until fully covered in the particle bed, and the vane was set to rotate at a constant rate of 0.5 rpm. For each sample, an average of 25 measurements was taken at different locations across the sample surface to ensure representative values and to avoid bias from local weakening caused by repeated measurements at the same location.

2.4 | Erosion by impinging jet experiments

The erosion experiments were conducted in a 0.5 × 0.5 × 0.5 m^3 impinging jet tank, which was sufficiently large to minimize the effects of flow recirculation.[18] The jet line was in the middle of the tank. The jet was connected to a 520 s peristaltic pump (Watson Marlow, UK) operating at its maximum operating speed (220 rpm) from a feed tank to the impinging jet tank. The impinging jet had an overflow port to avoid any overflow while the jet was in operation. The volumetric flow rate associated with the 220 rpm speed was measured at 3.04 L/min.

15475905, 2026, 6, Downloaded from https://aiche.onlinelibrary.wiley.com/doi/10.1002/aic.70336 by University Of Leeds The Brotherton Library, Wiley Online Library on [28/05/2026]. See the Terms and Conditions (https://onlinelibrary.wiley.com/terms-and-conditions) on Wiley Online Library for rules of use; OA articles are governed by the applicable Creative Commons License

Particle	d_{10} (μm)	d_{50} (μm)	d_{90} (μm)	d_{mean} (μm)	SD	CV (%)
H8	437	543	663	569	100	18
H9	301	382	488	404	79	20
H12	165	208	262	220	42	19
H16	65	85	110	91	20	22
H22	23	35	53	42	14	33

TABLE 1 10th percentile (d_{10}), median (d_{50}), 90th percentile (d_{90}), mean (d_{mean}), standard deviation (SD) and coefficient of variation (CV %) of the Honite glass particles.

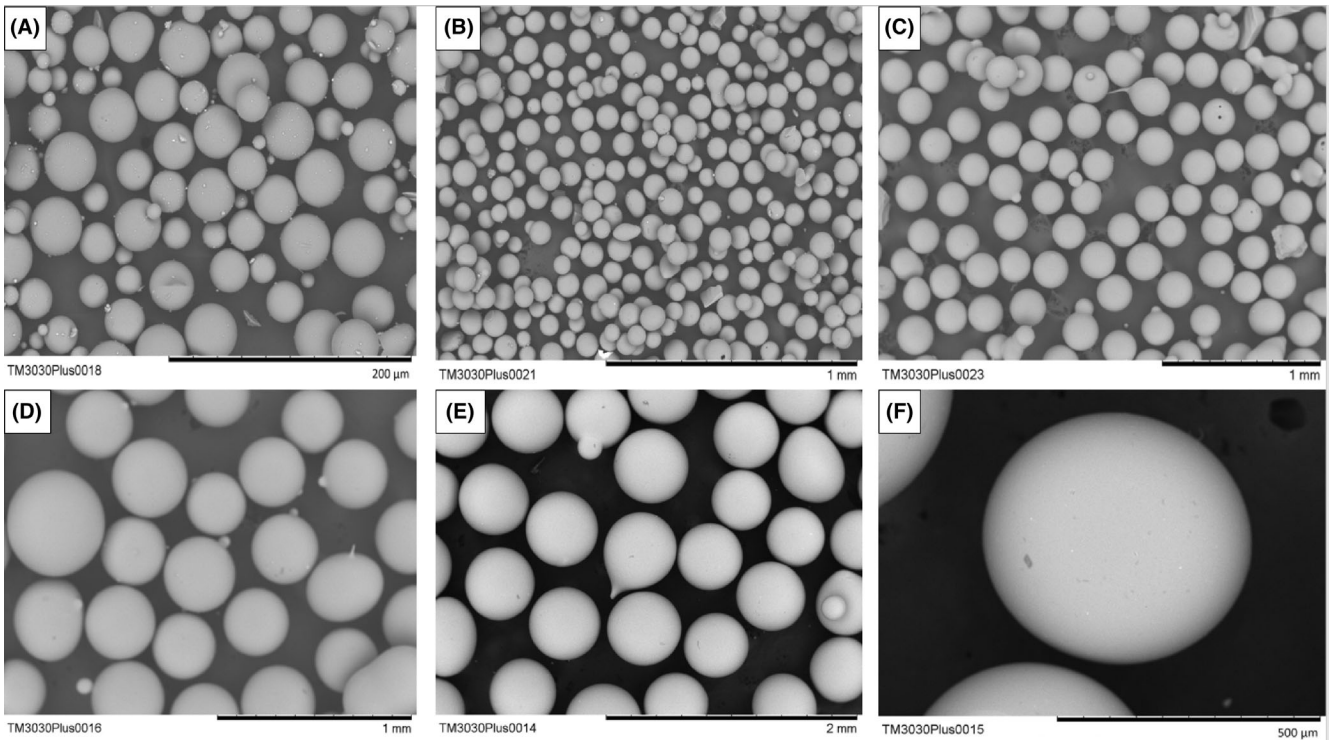

FIGURE 2 Images of the Honite glass particles using the scanning electron microscope: (A) H22; (B) H16; (C) H12; (D) H9; (E) H8; (F) H8 single particle.

The jet had 8 interchangeable nozzles, ranging from 3 mm to 10 mm. The velocity (U) associated with each nozzle diameter can be determined using the following relation:

$$U = \frac{4\dot{V}}{\pi D^2}, \quad (2)$$

where $\dot{V}$ is the volume flow rate (m^3/s), and D is the nozzle diameter (m). Table 2 summarizes the velocities and Reynolds numbers for the different jet nozzle diameters tested associated with a 3.04 L/min flow rate. In all cases, the jet was higher than the lower limit of the turbulent flow regime (Re >3000).[40]

The tank was filled with water to a height of 0.4 m (corresponding to a volume of 100 L), and the jet was fully submerged. For each experiment, a bed of flat Honite particles with a thickness of ~30 mm was prepared, which for the higher jet velocities meant the sediment bed was entirely cleared beneath the jet zone. However, a larger bed thickness was not selected as the small bed thickness more accurately represents the conditions within the HASTs.[7] The Honite particles were thoroughly mixed, allowed to settle, and made level to create a uniform bed. The jet was run for 90 s for each experiment, which was determined by initial testing and image analysis to be sufficient to reach a steady state crater profile. This jet running time is consistent with the jets in the HASTs which run on short firing periods of 45–90 s.[8] It is noted that there is a possibility of ongoing erosion over very long periods of time. However, since the erosion process follows an exponential decay, most of the erosion happens in a very short time early in the process.[41]

For each Honite type, all the jet diameters mentioned in Table 2 were tested (3–10 mm). For H8, H9 and H12, the tested jet heights from the bed (h) were $h = 10D$, $20D$, $30D$ and $40D$ (D = jet diameter) for $D = 3$–6 mm, and $h = 10D$ and $20D$ for $D = 7$–10 mm. Finally, for the smaller particles, H16 and H22, $h = 10D$ and h = $20D$ were tested for $D = 3$–10 mm. Crater radius measurements were obtained manually using a graduated scale mounted on a rigid rod. Each of the measurements was repeated 2–5 times and an average taken. The bed was reset and prepared again after each run.

15475905, 2026, 6, Downloaded from https://aiche.onlinelibrary.wiley.com/doi/10.1002/aic.70336 by University Of Leeds The Brotherton Library, Wiley Online Library on [28/05/2026]. See the Terms and Conditions (https://onlinelibrary.wiley.com/terms-and-conditions) on Wiley Online Library for rules of use; OA articles are governed by the applicable Creative Commons License

TABLE 2 Velocities and Reynolds number (*Re*) associated with the jet nozzle diameters tested.

Jet diameter (m)	Velocity (m/s)	*Re*
0.003	7.18	21,530
0.004	4.04	16,148
0.005	2.58	12,918
0.006	1.79	10,765
0.007	1.32	9227
0.008	1.01	8074
0.009	0.80	7177
0.010	0.65	6459

The clearance effect of the jet, quantified by the clearance radius, was captured using a camera positioned underneath the tank, as shown in Figure 3. Here, the clearance radius is defined as the radial distance from the jet centerline to the outermost location on the tank base where particles were completely removed while the jet was operating (i.e., the cleared region). Video recording started when the jet began running and continued until the jet was turned off. The video was analyzed to establish the temporal evolution of erosion and to measure the clearance radius. The dynamic steady-state clearance radius (jet on) was measured using ImageJ (National Institute of Health, USA),[42] an image processing and analysis software program. The ImageJ spatial calibration was obtained using the known distance between the inner edges of the tank, allowing conversion from pixels to millimeters. The measurement precision was estimated from five repeated ImageJ measurements of the clearance area for the same frame, giving an uncertainty in the derived clearance radius of approximately ±0.4 mm (one standard deviation).

2.5 | Light detection and ranging (LiDAR)

Several measurements were taken using LiDAR to assess its efficacy for capturing the full crater profiles (H9, $D = 7$–10, $h = 10D$). LiDAR was used to produce a three-dimensional reconstruction of the crater, allowing for the study of its shape and the measurement of its depth and radius. LiDAR, short for light detection and ranging, is a sensing technology that operates similarly to radar but uses light instead of radio waves. The LiDAR measurements in the experiments were taken using an iPhone 12 Pro (Apple, USA). The iPhone LiDAR system has recently been adopted in geosciences and other three dimensional mapping applications due to its versatility, relatively high accuracy, and cost-effectiveness.[43,44]

Using LiDAR in water can be challenging due to limitations such as refraction and light absorption. Therefore, for the LiDAR measurements, the tank was fully drained by reversing the flow direction of the pump. Draining had to be done carefully when reaching a low water level to avoid altering or collapsing the crater. Therefore, a squeeze bottle or syringe was used to carefully drain the water around and inside the crater. The crater was scanned by moving the iPhone around it, capturing it from different angles. The application used for LiDAR data capturing and processing was Scaniverse (Niantic, Inc., USA). The LiDAR data were then exported as an OBJ file to Inventor (Autodesk, USA), a three-dimensional CAD software, to perform crater size measurements.

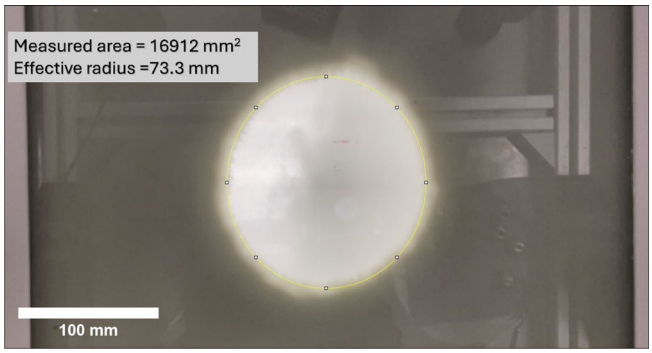

FIGURE 3 Example of erosion/clearance captured from underneath the tank while the jet is engaged (H16, $D = 4$ mm, $h = 10D$). ImageJ was utilized to measure the clearance area. Pixel distance was correlated to the measured physical distance between the inner edges of the tank.

2.6 | Ultrasonic velocity profiler (UVP)

A UVP-DUO ultrasonic velocity profiler (Met-Flow, Switzerland) was employed as a non-intrusive method to scan and measure the steady state crater profiles for H9, H12, and H16 ($D = 3$–6 mm, $h = 10D$ and $20D$), and for H22 ($D = 3$–6 mm, $h = 10D$). The UVP determines particle velocities in the flow by analyzing the Doppler frequency shift of transmitted acoustic pulse echoes, a method well documented in the literature.[45] It also detects the presence of solid surfaces and beds by measuring the intensity of backscattered echoes at various depths, which is how it was utilized in this study. The UVP system used consisted of a 5 mm diameter, 2 MHz transducer head (probe) connected to a controller box that communicated between the transducer and the UVP software. Table 3 provides a summary of the implemented UVP measurement parameters. The equivalent channel distance and width ensured no signal overlapping. The 0.74 mm channel size provided the required accuracy while still being larger than the individual particle size.

To use the UVP as a bed scanner, it was attached to a high-resolution traverse system (Dantec Dynamics, Denmark) via an arm constructed from aluminum. The UVP probe was secured inside a holder mounted at the end of this arm. After turning off the impinging jet, the jet was moved upwards, and the UVP was positioned directly beneath the jet centerline. The traverse then moved the UVP probe across the crater from the jet centerline toward the edge of the tank, allowing it to take measurements and scan the static steady-state crater profile as illustrated in Figure 4. The UVP probe was positioned 110 mm above the tank bottom and perpendicular to it. The UVP maximum measuring distance extended slightly beyond the tank

15475905, 2026, 6, Downloaded from https://aiche.onlinelibrary.wiley.com/doi/10.1002/aic.70336 by University Of Leeds The Brotherton Library, Wiley Online Library on [28/05/2026]. See the Terms and Conditions (https://onlinelibrary.wiley.com/terms-and-conditions) on Wiley Online Library for rules of use; OA articles are governed by the applicable Creative Commons License

bottom to ensure the entire depth was covered and to receive a backscatter signal when the echoes hit the tank bottom in cases where the particles were fully cleared.

The traverse moved at a speed of 1 mm/s, with the UVP beginning to record data simultaneously with the traverse's movement and stopping when the traverse halted. In this study, the UVP was utilized by analyzing the raw data of backscattered echo amplitude. The intensity of the backscattered signal indicates the location of the bed. As the pulse travels downward toward the bed, suspended sediments scatter some of the sound back, while the bed surface typically reflects a strong echo.

A MATLAB (MathWorks, USA) code was developed to analyze the raw echo amplitude data and convert it into a bed/crater profile. With a sampling period of 40 ms, 25 raw echo amplitude data profiles were measured every second. The raw data were exported to MATLAB, where they were averaged every second using the Root Mean Square (RMS) function. The MATLAB code processed each of the averaged profiles, automatically identifying the amplitude peaks that indicated the vertical distance of the bed surface from the UVP probe. Each averaged profile corresponded to the bed depth for a 1 mm horizontal distance, given the traverse speed of 1 mm/s. By determining the vertical distance of the bed surface for each horizontal position, the data were combined to construct and plot a crater profile. A rolling average with a window size of 15–20 and an outlier filter based on a threshold of 2 moving standard deviations were applied to smooth the profiles.

TABLE 3 UVP measurement parameters summary.

Signal parameters	Frequency	2 MHz
	Cycles	2
	Repetitions	128
	Noise level	4
	Sound speed	1475 m/s
Profile definition	Number of channels (bins)	165
	Number of profiles	3750–4750
	Sampling period	40 ms
Windows parameters	Channel distance	0.74 mm
	Channel width	0.74 mm
	Min-Max measurement distance	0.74–121.69 mm
Voltage and echo gain	Voltage	30 V
	Gain start-end	6–6

3 | RESULTS AND DISCUSSION

3.1 | Yield shear strength of particles

Figure 5 illustrates the mean yield stress of the Honite glass particles: H8, H9, H12, H16, and H22. It shows that the largest size distribution (H8) has the highest yield stress, with yield stress decreasing as particle size decreases. This trend reverses at H16, where the smaller particles (H22) exhibit a higher yield stress than H16. The reduction in yield stress with decreasing particle size occurs because larger particles require more force to move due to their higher inertia and mass per particle.[46] On the other hand, for smaller particles, typically below 100 μm, inter-particle forces become important and play a significant role relative to gravitational forces.[11,47] These cohesive forces, such as van der Waals and electrostatic forces, start to contribute to controlling the incipient motion of particles at these scales. Thus, the observed increase in yield stress for H22 can be attributed to the emergence of these interparticle forces.

Another factor that may contribute to the increased yield stress in H22 is its broader size distribution, which allows the smaller particles to fill the gaps between larger ones, enhancing interparticle interactions.[48] Louati et al.[49] investigated the shear behavior of two sets of wet, mono-sized glass beads (12–40 μm and 70–110 μm) and found that the smaller particles exhibited more cohesive behavior

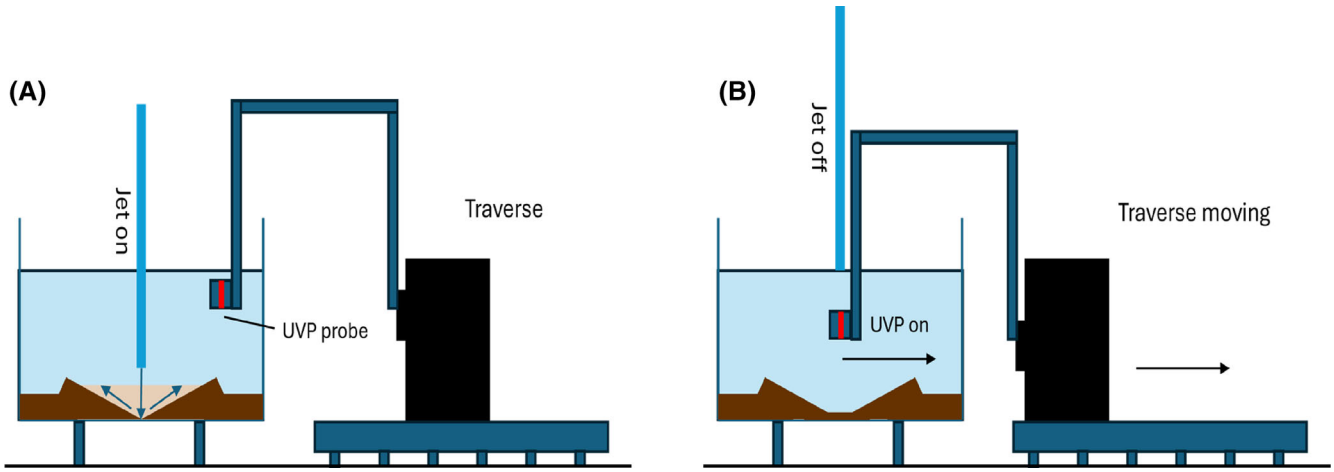

FIGURE 4 Schematic of UVP measurement process: The jet is on, and erosion is taking place (A), and the UVP is scanning the static steady-state crater profile starting from the jet centerline (B).

15475905, 2026, 6, Downloaded from https://aiche.onlinelibrary.wiley.com/doi/10.1002/aic.70336 by University Of Leeds The Brotherton Library, Wiley Online Library on [28/05/2026]. See the Terms and Conditions (https://onlinelibrary.wiley.com/terms-and-conditions) on Wiley Online Library for rules of use; OA articles are governed by the applicable Creative Commons License

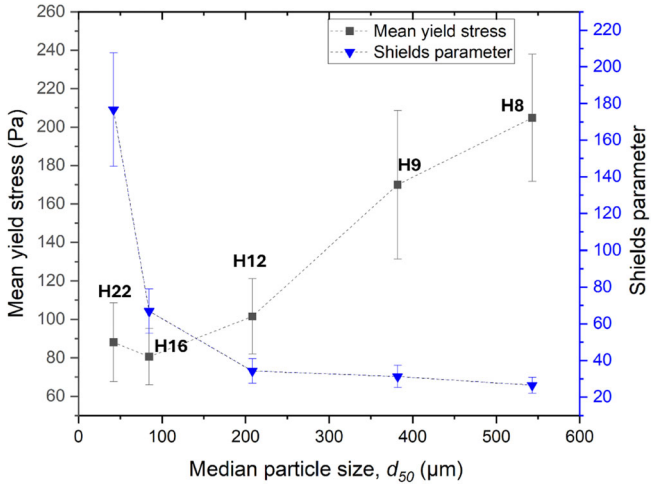

FIGURE 5 Mean yield stress (black squares) and critical Shields number (Blue triangles) of the Honite glass beads: H8, H9, H12, H16, H22 at 60% volume fraction. The error bars represent the standard deviation of the measurements.

and higher shear yield stress at a given liquid fraction. The median particle sizes in their study are comparable to those of H22 and H16 sizes, though their samples were more mono-sized than H22. This suggests that the increased yield stress in H22 is likely predominantly due to stronger inter-particle cohesive forces rather than its polydispersity. To summarize, Figure 5 shows a decrease in yield stress with decreasing particle size until a size threshold is reached, beyond which yield stress increases again for the smallest particles due to enhanced interparticle forces and cohesion. Similarly, Hao et al.[50] found that particles below a certain threshold, about 150 μm, exhibit an increase in bulk cohesion, while particles above this threshold show a considerable increase in bulk friction. In addition, Lick et al. (2004)[10] investigated the initiation of motion of granular quartz particles (5–1350 μm) and found that larger particles behaved non-cohesively, whereas finer particles transitioned into cohesive behavior. This transition was reflected in the measured critical shear stress, which exhibited a minimum at around 100 μm and then increased for smaller particles as cohesive forces became significant.

The error bars, particularly for the larger particles, represent the standard deviation across repeated measurements. The observed variability may be attributed in part to the use of the smallest vane, which reduces the sheared surface area compared with larger vanes and increases measurement uncertainty.[51,52] In addition, vane viscometer measurements are highly sensitive to solid fraction, especially at the high concentrations characteristic of packed spherical granular beds. Under these conditions, the yield stress can change sharply with small variations in local solid fraction. Therefore, spatial variations in packing, particularly at shallow depths given the small vane size, can contribute to the variations in the measured yield stress. Such variability is expected given the system nature and has been reported in the literature.[52,53] To address this issue, a substantial number of measurements were taken in the present work.

Figure 5 also shows the critical Shields number of the different Honite size distributions. The critical Shields number here is[54]:

$$Sh_c = \frac{\tau_c}{(\rho_s - \rho_f) g (d_{50})}, \tag{3}$$

where τ_c is the critical bed shear stress at incipient motion (Pa) obtained by the vane viscometer, d_{50} is the particle median size (m), and ρ_s and ρ_f represent the densities of the particle and the fluid (kg/m^3), respectively. The critical Shields parameter represents a balance between the forces acting on the sediment: the shear stress exerted by the fluid and the weight of the particles. It is used to describe the initiation of erosion for sediments of different sizes.[55]

In an impinging jet, the flow approaches the bed with predominantly axial momentum in the free-jet region. Following jet–bed interaction in the impingement region, the bed surface deforms as erosion initiates, and the flow is deflected and rapidly redirected into a near-bed radial wall jet. As a result, erosion is governed primarily by the bed shear stress applied by this near-bed flow, which must overcome the bed's resisting shear strength. The yield shear stress measured using the vane viscometer represents the minimum stress required to initiate movement of the bed material,[38,53] and is therefore considered here as an estimate of τ_c for the purpose of evaluating Sh_c. Figure 5 shows an increase in the critical Shields number for the smallest Honite particles, H22, compared to the other Honite particles. This increase has been observed in the literature for fine sediments, where internal cohesive forces between particles begin to emerge.[23,55,56] The change suggests that significant internal cohesive forces start to appear between H16 and H22, given the inflection in the Shields number trend in this region.

3.2 | Influence of jet height, velocity and particle size on erosion

The effect of jet height on the erosion of the Honite glass beads H8, H9 and H12 was studied for jet heights between 10*D* and 40*D*, where *D* is the jet diameter. The jet diameters used were between 3 mm and 6 mm corresponding to velocities between 7.18 and 1.79 m/s, respectively (Table 2). Final measured steady-state crater diameters for H12 glass particles are compared in Figure 6. Crater-radius measurements were highly repeatable, with associated uncertainties that were small; therefore, error bars are omitted from Figures 6, 7, and 10 to maintain figure clarity, and corresponding error bars for a representative case (Figure 6) are shown in the Electronic Supplementary Materials (ESM) Figure S1.

For $D = 5$ mm ($U = 2.58$ m/s) and $D = 6$ mm ($U = 1.79$ m/s), the crater diameter increases with increasing jet height until it reaches a maximum value and then starts decreasing. The observed trend is consistent with the literature.[57,58] For higher velocities at $D = 3$ mm and $D = 4$ mm, the crater diameter continues to increase with increasing jet height (Figure 6), however, it should eventually reach a peak at higher jet heights ($h/D > 40$), following the trend in the

15475905, 2026, 6, Downloaded from https://aiche.onlinelibrary.wiley.com/doi/10.1002/aic.70336 by University Of Leeds The Brotherton Library, Wiley Online Library on [28/05/2026]. See the Terms and Conditions (https://onlinelibrary.wiley.com/terms-and-conditions) on Wiley Online Library for rules of use; OA articles are governed by the applicable Creative Commons License

$D = 5$ mm and $D = 6$ mm results. The jet height at which the peak occurs increases with the nozzle jet velocity. The same trend is observed for H8 and H9 particles and is provided in the ESM Figure S2.

This trend is related to the balance between the interaction velocity of the jet with the bed and the total entrained volume of the jet at the bed surface. As the jet is raised higher above the bed, the shear velocities at the bed interface decrease. However, the overall interaction area between the jet and the bed increases. More liquid will be entrained in a self-similar manner in the free-jet region and thus in the impingement zone when the jet is lifted higher from the bed.[59] At a certain height, the interaction velocity between the jet and the bed becomes insufficient to erode the bed, leading to a reduction in overall erosion. The impinging jets inside the nuclear HASTs have been designed to be positioned about 10*D* from the base of the tank to increase the impact velocities on the bed.[18] However, this design suggests that the jet-bed interaction volume will be small, which may lead to a reduction in potential erosion in the HAST systems, given the relatively high velocities used in these systems.

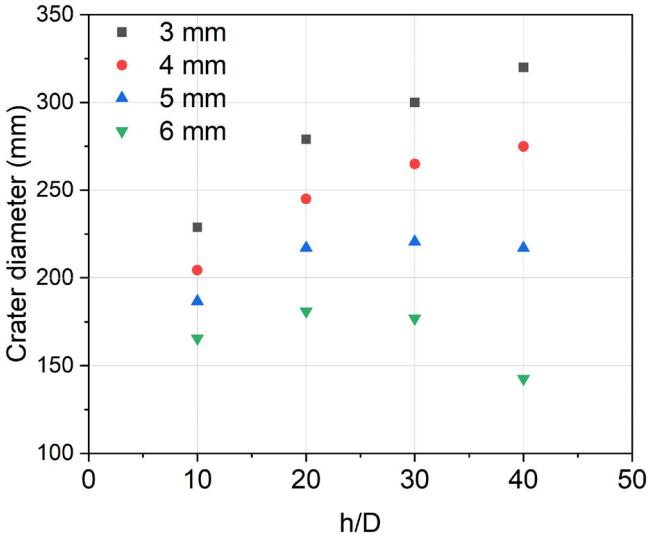

FIGURE 6 H12 Crater diameter (mm) vs. normalized jet height (*h*/*D*) for different jet nozzle diameters (*D*, mm).

The effect of jet nozzle velocity and particle size on jet erosion was considered for all five Honite glass particles distributions (H8, H9, H12, H16, and H22), with jet diameters varied between 3 mm and 10 mm corresponding to velocities between 7.18 and 0.65 m/s (Table 2). The steady-state static crater diameter measurements are summarized in Figure 7 for set jet heights of 10*D* (A) and 20*D* (B). The general trend observed is that the steady-state crater diameter decreases as the jet diameter increases. Given that the flow rate of the jet is constant, a larger jet diameter corresponds to a lower nozzle velocity and a reduced Reynolds number, as shown in Table 2. Although a larger diameter increases the interaction area at the bed, the reduction in Re and the lower impact velocity at the bed interface have the dominant effect. Consequently, this leads to less erosion. For some particle sizes (Figure 7A, $h = 10D$), the crater diameter began to slightly increase with larger jet diameters. However, at these lower speeds, the crater radius alone may not be a sufficient indicator of erosion, as the craters became flatter with ill-defined crater peaks (i.e., the ring formed around the crater from material uplifted along the crater's walls).

At a given jet speed and height, H8, which has the largest particle size distribution, has the smallest crater diameters. Following this, H9, H12, and H16 show respectively larger crater diameters. This indicates a trend where larger particle sizes result in less erosion. This trend occurs because larger particles have higher inertia and mass, requiring more force to move them, thus resulting in less erosion. However, H22, with the smallest particle size, clearly deviates from this trend and does not have the largest crater diameters. This deviation is likely due to the increasing significance of inter-particle forces at such small particle size distributions, which reduces erosion. This explanation aligns with the yield stress measurements shown in Figure 5, where H22 similarly deviates from the trend of increasing

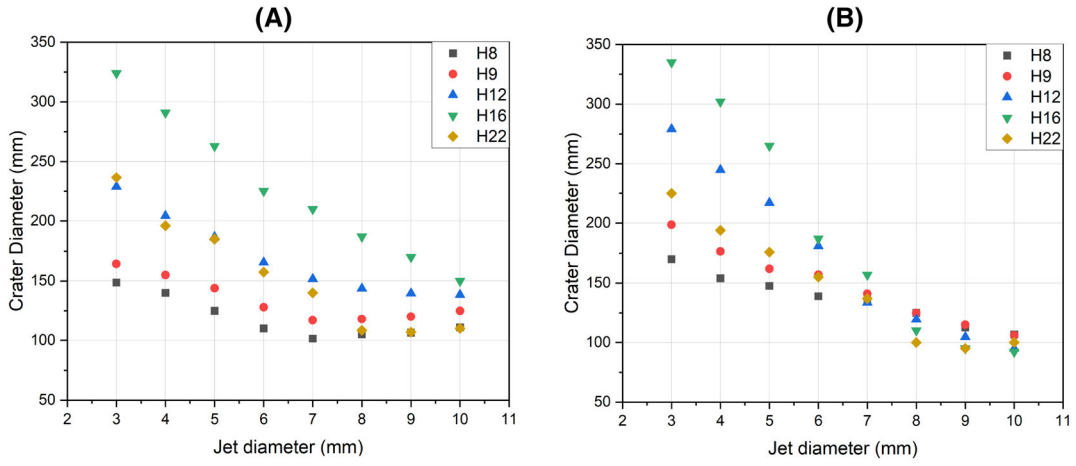

FIGURE 7 Honite glass particle crater diameter vs. jet diameter at $h = 10D$ (A) and $h = 20D$ (B).

15475905, 2026, 6, Downloaded from https://aiche.onlinelibrary.wiley.com/doi/10.1002/aic.70336 by University Of Leeds The Brotherton Library, Wiley Online Library on [28/05/2026]. See the Terms and Conditions (https://onlinelibrary.wiley.com/terms-and-conditions) on Wiley Online Library for rules of use; OA articles are governed by the applicable Creative Commons License

yield stress with increasing particle size. Indeed, for the greater 20*D* height, the erosion crater diameter for the smallest H22 particles is considerably lower than the larger H16 and H12 particles, at least for the smaller nozzle diameters.

When comparing the crater diameters at $h = 10D$ (A) and $h = 20D$ (B) in Figure 7 for a specific particle size, it is evident that for small jet diameters, the crater diameters at $h = 20D$ are larger than those at $h = 10D$. However, at higher jet diameters, this trend reverses, with the crater diameters at $h = 10D$ becoming larger than those at $h = 20D$. Again, this trend is due to the balance between the interaction velocity and the entrained volume of the jet at the bed interface, as explained earlier. For instance, the crater diameters of H16 at $h = 20D$ are larger than those at $h = 10D$ until a jet diameter of 6 mm is reached, at which point the crater diameter at $h = 10D$ becomes larger. Similarly, for H12, this reversal occurs at a jet diameter of 7 mm. The jet diameter at which this change occurs depends on the particle size: smaller particles experience this reversal at smaller jet diameters, as shown in the ESM (Figure S3). Interestingly, for the smallest particle size (H22), the crater diameters for both $h = 10D$ and $h = 20D$ are relatively close, with the $h = 10D$ crater diameter being slightly larger. This demonstrates that the optimal jet height depends on the properties and size of the particles. For finer particles, a relatively small jet height, such as $h = 10D$ as used in the HASTs, would be sufficient.

3.3 | LiDAR and UVP measurements of crater profiles

The LiDAR method was used to measure some H9 crater profiles at a jet height of 10*D* for $D = 7$–10. Figure 8 shows a three-dimensional reconstruction of the H9 crater created with LiDAR technology. The shape of the crater is consistent with cohesionless sediments described in the literature.[16,31,57] The maximum depth occurs at the center of the crater, with particles deposited around the crater, forming peaks that rise above the original bed level. The LiDAR crater profile data were analyzed to obtain size measurements, such as the diameter and depth of the crater. A cross-section was taken to extract these measurements, as illustrated in Figure 8.

The crater diameter values obtained using LiDAR for jet diameters $D = 7$, $D = 8$, and $D = 9$ mm closely match those measured manually (Table 4). The percentage difference is higher for the $D = 10$ measurement, but it remains within an acceptable range, demonstrating the accuracy of the LiDAR measurements. One challenge associated with the LiDAR technique is that the tank must be drained of water. Draining has to be performed slowly and carefully to avoid altering the depth and shape of the crater. Rapid liquid extraction in the vicinity of the crater can cause the crater to collapse, resulting in inaccurate depth measurements. Considering this challenge, UVP was selected for further profile analysis. However, LiDAR demonstrated its accuracy in measuring crater diameter and is recommended for more suitable studies involving systems without water, such as air jet erosion.

Crater profiles from Honite glass beads (H9, H12, H16, H22) were measured using the UVP traverse system for $D = 3$–6 mm (with velocities of 7.18–1.79 m/s) and jet heights of 10*D* and 20*D*, as illustrated in Figure 9. The profiles are shown relative to the tank base, set as the zero-depth reference, and the original sediment level is approximately 30 mm. The profiles in Figure 9 represent the steady-state static crater profiles where the UVP measurements were taken after the jet was disengaged and the particles had settled. This settling occurs quickly once the jet is turned off. The profiles were scanned starting from the jet centerline and moving outward toward the tank

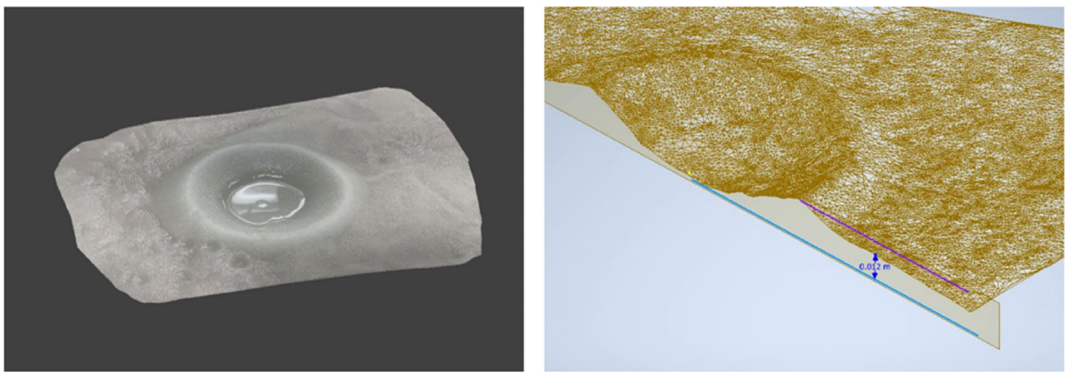

FIGURE 8 Three-dimensional reconstruction of H9 crater using LiDAR, $D = 10$ (left), a cross section through the middle of the crater (right).

TABLE 4 Comparison of crater diameters measured manually and using LiDAR for H9, $D = 7$–10 at $h = 10D$.

Jet diameter, *D* (mm)	Crater (manual) (mm)	Crater (LiDAR) (mm)	% difference
7	117	118.5	1.27
8	118	117	0.85
9	120	121	0.8
10	125	117.5	6.18

15475905, 2026, 6, Downloaded from https://aiche.onlinelibrary.wiley.com/doi/10.1002/aic.70336 by University Of Leeds The Brotherton Library, Wiley Online Library on [28/05/2026]. See the Terms and Conditions (https://onlinelibrary.wiley.com/terms-and-conditions) on Wiley Online Library for rules of use; OA articles are governed by the applicable Creative Commons License

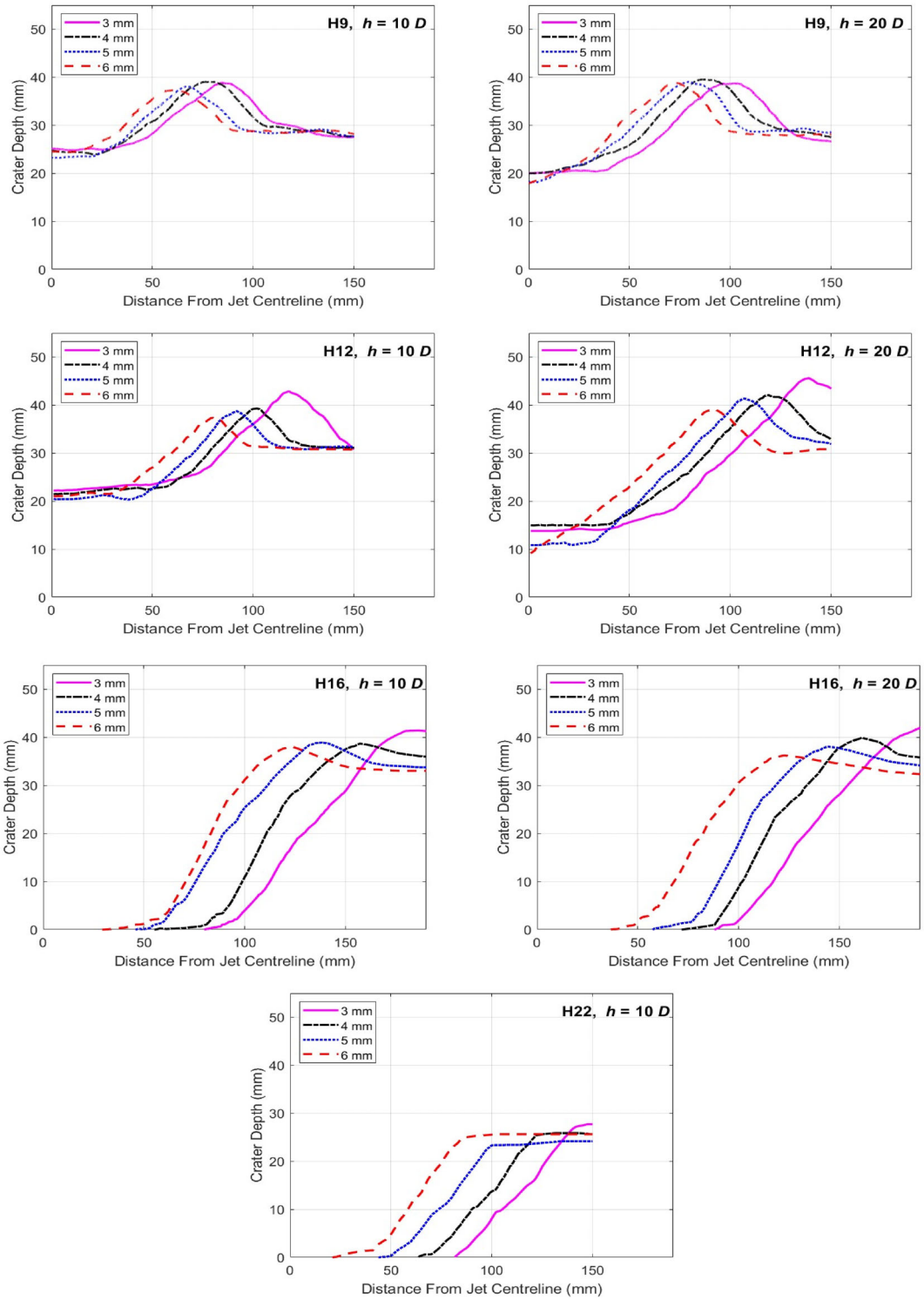

FIGURE 9 Steady-state static crater profiles measured by the UVP for the Honite glass particle: H9, H12 and H16 (top to bottom) at different jet heights, h: 10D (left) and 20D (right). The legend indicates the jet diameter, D, ranging from 3 mm (7.18 m/s) to 6 mm (1.79 m/s). H22 measurements were taken for $h = 10D$ only.

wall, representing half of the crater. The crater was assumed to be symmetrical, an assumption confirmed by both LiDAR scans and manual measurements. To assess the accuracy of the UVP crater profiles, the radii of the craters obtained by the UVP were compared to manual measurements, with the percentage differences falling within an acceptable range. A further comparison between the steady-state static clearance radius for H16 and H22 measured by image analysis and the UVP is provided in the ESM (Table S1). Additionally, the

15475905, 2026, 6, Downloaded from https://aiche.onlinelibrary.wiley.com/doi/10.1002/aic.70336 by University Of Leeds The Brotherton Library, Wiley Online Library on [28/05/2026]. See the Terms and Conditions (https://onlinelibrary.wiley.com/terms-and-conditions) on Wiley Online Library for rules of use; OA articles are governed by the applicable Creative Commons License

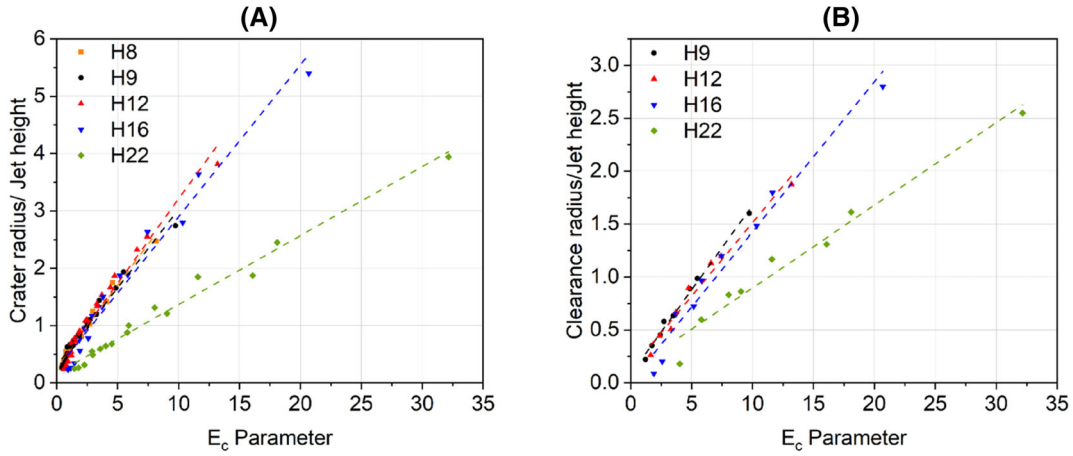

FIGURE 10 Normalized crater radius (A), representing the static steady-state crater radius, and normalized clearance radius (B), representing the dynamic steady-state clearance radius of the tank base (B) against E_c parameter.

overall shape of the UVP profiles was comparable to the craters' visual appearance, further confirming the accuracy.

It is important to note that, for all heights and velocities presented, the jet completely penetrated the sediment bed and reached the tank bottom (the zero-depth reference) when engaged (jet on). This behavior was confirmed by a camera positioned underneath the tank, as shown in Figure 3. This full penetration occurred even for H9 and H12, although this may not be evident in their steady-state static crater profiles presented in Figure 9. Following jet disengagement (jet off), the H9 crater profiles indicate that many particles resettled within the crater. H12 also experienced resettlement, but with fewer particles than H9 due to its smaller particle size and lower resistance, leading to deeper craters for H12. In contrast, the crater profiles for the finer particles, H16 and H22, show a consistent clearance radius, where particles did not resettle near the crater center but were pushed further away by the flow.

The flow patterns within craters created by impinging jets have been classified by Aderibigbe and Rajaratnam[16] into two main regimes as noted earlier: the Weakly Deflected Jet Regime (WDJR) and Strongly Deflected Jet Regime (SDJR). In the WDJR, the jet weakly penetrates the bed, resulting in a reduced interaction and shallow craters, which is mainly associated with a low erosion parameter (E_c <0.35). In contrast, in the SDJR, the flow strongly penetrates the sediments and deflects within the crater leading to recirculatory flow. Several clockwise and counterclockwise vortices can develop within the craters, as described in recent studies.[60,61] These vortices interact with the sediment bed, entraining some particles into suspension and maintaining them within the recirculating flow, while also transporting other particles outward toward the inner sides of the crater, where deposition occurs at larger radial distances.

The crater profiles illustrated in Figure 9 are mainly a result of the particle size, which influences not only the crater size and shape but also the resettlement behavior and interaction with the flow. At the given velocities and jet heights shown in Figure 9, the jet experienced strong deflection and recirculation within the crater, with an erosion parameter E_c well above 0.35, consistent with the SDJR. For the larger particles (H9, H12), particles tend to resettle more quickly once entrained and are less readily transported outward by the recirculating vortex flow within the crater. As a result, these particles are more prone to resettle within the crater compared with the finer particles (H16 and H22). When the jet was engaged, a portion of the particles became trapped in the recirculating flow within the crater, forming a cloud-like dispersion zone within the crater. These particles resettled into the crater once the jet was disengaged. Larger particles, such as H9, were more likely to be trapped within the crater and resisted being pushed away by the flow given their higher inertia. This resistance contributed to the formation of larger crater peaks, which in turn intensified the recirculation within the crater. The mutual influence and interaction between the flow and the crater morphology described is consistent with previous work.[19,62] The enhanced recirculation led to higher particle resettlement within the crater, resulting in a lower crater depth. On the other hand, the finer particles (e.g., H16) exhibited less resistance to the flow, leading to smaller crater peaks and greater clearance from the crater due to lower recirculation.

As illustrated in Figure 9, for H9 and H12 at the given velocities, a jet at a height of 20D consistently produced craters with a larger radius than a jet at a height of 10D, consistent with the discussion in Section 3.2. Additionally, Figure 9 highlights another key point; jet height significantly influenced particle clearance and resettlement, which in turn affected the depth of the crater. Generally, deeper craters were formed at a jet height of 20D compared to 10D, which is not necessarily correlated with crater size. For instance, even the smallest crater created at 20D ($D = 6$ mm) is deeper than the largest crater formed at 10D ($D = 3$ mm). The jet height influences both the interaction velocity of the jet with the bed and the total volume of fluid impacting the bed surface, which in turn affects the intensity of the flow and the recirculation patterns within the crater. The higher jet height of 20D led to a larger volume and overall interaction area with the bed, thereby

15475905, 2026, 6, Downloaded from https://aiche.onlinelibrary.wiley.com/doi/10.1002/aic.70336 by University Of Leeds The Brotherton Library, Wiley Online Library on [28/05/2026]. See the Terms and Conditions (https://onlinelibrary.wiley.com/terms-and-conditions) on Wiley Online Library for rules of use; OA articles are governed by the applicable Creative Commons License

increasing the particle erosion. However, further increasing the jet height would eventually reduce the impact velocity to a degree that outweighs the benefit of the increased interaction area, leading to decreased particle erosion and, consequently, a lower crater height, as shown in previous studies.[16,18]

A consistent trend observed across all crater profiles of the Honite glass beads in Figure 9 is that crater size increases with decreasing jet diameter. Given that the jet flow rate is constant, a smaller jet diameter corresponds to a higher nozzle velocity and Reynolds number. Although a smaller diameter decreases the interaction area at the bed, the increase in impact velocity and Reynolds number has a dominant effect. Higher jet velocities increase compressional pressure and lateral shear forces, enhancing erosion based on a single-particle momentum balance. This increase in crater size also results in higher crater peaks, with H12 providing the clearest example. This aligns with findings from studies that examined crater profiles.[18,63,64] An additional observation regarding the peaks is that their size decreases as the Honite particle size decreases. For a given jet diameter, velocity, and height, H9 exhibits the largest peak size (both width and height), followed by H12, H16, and finally H22, which shows no peak formation. The presence of peaks is characteristic of cohesionless sediments, whereas cohesive sediments typically display very small peaks or none at all.[65] Therefore, based on the physical appearance of the crater, it can be inferred that H22 begins to exhibit cohesive behavior. Thus, the transition in peak formation from H9 to H22 not only highlights the role of particle size in sediment behavior but also suggests that H16 reaches a threshold where cohesive forces start to appear, altering its deposition pattern and aligning it more closely with the behavior of cohesive sediments.

3.4 | Normalized erosion data

The erosion of the glass particles can be normalized and modeled by implementing what is known as the erosion parameter, E_c, as considered byAderibigbe and Rajaratnam,[16] which is the ratio of the densimetric Froude number normalized with the jet height h/D ratio, as given by Equation (4):

$$E_c = \frac{U\left(\frac{D}{h}\right)}{\sqrt{gd\left(\frac{\rho_s - \rho_f}{\rho_f}\right)}}, \tag{4}$$

where U is the jet nozzle exit velocity (m/s), D is the jet diameter, h is the jet height from the original bed level (m), d is the d_{50} particle diameter (m), ρ_s is the particle density (kg/m^3), ρ_f is the fluid density (kg/m^3) and g is the gravitational acceleration (m/s^2). E_c can be viewed as an impinging-jet-specific analogue of the more general Shields number (Equation (2)). The fluid inertial shear stress can be expressed in terms of the nozzle exit velocity and fluid density as $\tau = \rho_f U^2$.[25,66] Accordingly, E_c can be related to Sh as follows: $E_c = (h/D)\sqrt{Sh}$. E_c provides a degree of normalization between systems with different jet and particle properties, allowing for direct comparison between them. Consequently, it has been frequently used in cohesionless impinging jet erosion studies.[18,19]

The normalized crater radius and clearance radius were modeled using the erosion parameter, as shown in Figure 10. The crater radius refers in this figure to the distance from the crater center to the crater peak and is normalized by the jet height. As described in previous sections, the crater measurements were taken after the jet was disengaged, representing the static steady-state radius. Figure 10A comprehensively includes all jet velocities listed in Table 2 and all jet heights discussed in Section 2.4. In contrast, the clearance radius is defined as the tank base radius to which particles were completely eroded while the jet was engaged, reflecting the dynamic steady-state clearance. This radius was observed by a camera positioned beneath the tank, where the jet's impact on the bottom surface was visible (as illustrated in Figure 3) and was measured using image analysis. The clearance radius data in Figure 10B include jet heights of 10D and 20D for jet diameters ranging from 3 mm to 6 mm.

Figure 10 shows that the normalized crater radius is linearly proportional to the E_c parameter for all Honite particles. This linear relationship is consistent with trends observed for cohesionless particles[16,18] for moderate to high flow velocities. Additionally, the data for H8 to H16 nearly collapse into a single relationship, indicating that these particles erode in a similar cohesionless manner and the model adequately normalizes their behavior. In contrast, H22 deviates from this pattern, exhibiting a less steep gradient compared to the other particles. Indeed, although H22 particles are the smallest, they did not produce the largest craters; instead, H16 formed the largest craters among the Honite types. This observation aligns with the yield stress data presented in Figure 5, where H16 exhibits the lowest yield stress, indicating the least resistance to the force exerted by the fluid and resulting in the highest erosion (crater radius). This correlation extends to the other Honite particles: the higher the yield stress, the less erosion occurs, as reflected in the largest value of the normalized erosion radius for each set of Honite particles. The deviation observed with H22 supports the yield stress data trend and suggests that at such small particle sizes, inter-particle forces and cohesion begin to play a more significant role. This behavior was also confirmed by the shape of the H22 craters produced by the UVP (as illustrated in Figure 9), where the H22 craters displayed no peaks, a characteristic of cohesive sediments.

Because of the breakdown of the relationship for the H22 data, owing to likely cohesion, an alternative method for modeling the erosion of Honite glass particles is proposed. This approach emphasizes the yield stress of the particle bed rather than focusing on individual particle properties such as size and density. The method is based on the force balance achieved at the steady-state crater, where the force exerted by the fluid equals the resistance force of the particle bed, that is, $\tau_f A = \tau_c A$. Since the impacted area (A) which is the bed interface, is the same on both sides of this equation, the shear stress exerted by the fluid on the particle bed (τ_f) is equal to the critical shear stress of the bed (τ_c) when a steady-state crater is reached.

15475905, 2026, 6, Downloaded from https://aiche.onlinelibrary.wiley.com/doi/10.1002/aic.70336 by University Of Leeds The Brotherton Library, Wiley Online Library on [28/05/2026]. See the Terms and Conditions (https://onlinelibrary.wiley.com/terms-and-conditions) on Wiley Online Library for rules of use; OA articles are governed by the applicable Creative Commons License

$$\tau_f = \tau_c. \tag{5}$$

The fluid applied shear stress can be approximated as:

$$\tau_f = \frac{c_f}{2}\rho_f u_{m,r}^2, \tag{6}$$

where c_f is the skin friction coefficient, ρ_f is the fluid density (kg/m^3), and $u_{m,r}$ is the maximum radial jet velocity in the vertical plane which is given by:

$$u_{m,r} = \frac{UDh_r}{r}, \tag{7}$$

where U and D are the mean jet nozzle exit velocity and nozzle diameter, respectively, r is the clearance/crater radius and h_r is the turbulent radial wall jet velocity decay coefficient.[6,67] Substituting Equation (7) and Equation (6) into Equation (5) gives:

$$r = kUD\sqrt{\frac{\rho_f}{\tau_c}}, \tag{8}$$

where $k = c_f h_r^2/2$ which can be found experimentally. A similar equation was derived by Hamm et al.[21] for the cleaning radius of a wall jet rather than an impinging jet, in the normalization of erosion from cohesive nuclear wastes. In the present work, Equation (8) is normalized by the jet height (h) that then leads to non-dimensionalization. After normalization, a new parameter, the critical shear stress erosion parameter (E_τ), is defined:

$$\frac{r}{h} = kE_\tau, \qquad E_\tau = U\frac{D}{h}\sqrt{\frac{\rho_f}{\tau_c}}. \tag{9}$$

The non-dimensional E_τ parameter can be viewed as the ratio of the fluid-applied shear stress to the critical bed shear stress. This formulation is motivated by the fact that, upon impingement, the jet is progressively deflected from a predominantly vertical flow into a near-bed radial wall jet, such that sediment mobilization is governed primarily by shear stresses acting along the bed surface. Accordingly, τ_c represents the critical bed shear resistance, estimated here as the mean yield shear stress measured using the vane viscometer.

The application of the newly defined erosion parameter E_τ to the Honite erosion data is illustrated in Figure 11. Both the normalized crater radius and normalized clearance radius show a linear relationship with E_τ for all Honite particle types. As shown in Figure 11A, the gradients of the linear fits of H8, H9, H12 and H22 range from $k = 1.5$–1.7 indicating a small amount of scatter. H16 exhibits a slightly higher gradient ($k = 2.1$), which may be attributed to H16 having the lowest yield stress, at which point a threshold between particle size and yield stress appears to be reached, as shown in Figure 5. Nevertheless, the relative scatter of the gradients, including H16, as quantified by the coefficient of variation of the gradients is 13.2%, which indicates a low scatter that remains within the error range of the yield stress measurements given in Figure 5. Similarly, the gradients of the linear fits in Figure 11B are of low scatter, ranging from $k = 0.81$–1.08 with a coefficient of variation of 11.8%. A closer look at Figure 11B shows a slight separation between the smaller particles (H16, H22) and the larger particles (H9, H12). This slight separation may reflect the behavior of the particle craters in regions, where the larger ones with higher inertia and yield stress had a higher resistance of the flow and collapsed back into the crater when the jet was disengaged. On the other hand, the smaller particles did not fully collapse back, resulting in a static consistent clearance area, as shown by Figure 9.

The large separation between the H22 erosion data and the other Honite particle data observed when using the standard erosion parameter E_c, as shown in Figure 10, is eliminated when E_τ is used for modeling, as shown in Figure 11. Since E_τ incorporates the yield shear stress of the material, it effectively captures the transition to cohesive

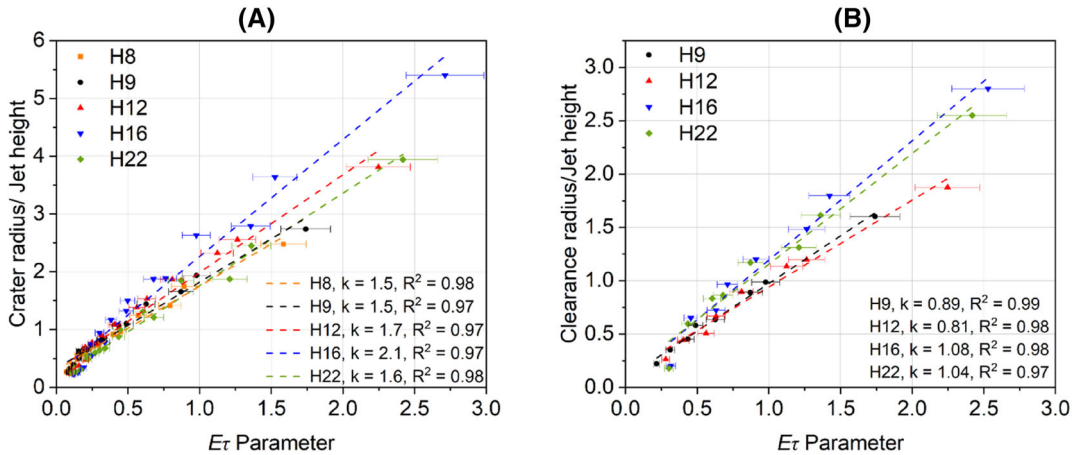

FIGURE 11 Normalized crater radius (A), representing the static steady-state crater radius, and normalized clearance radius (B), representing the dynamic steady-state clearance radius of the tank base, vs. E_τ parameter. Error bars show the standard deviation in E_τ due to yield-stress measurement variability.

15475905, 2026, 6, Downloaded from https://aiche.onlinelibrary.wiley.com/doi/10.1002/aic.70336 by University Of Leeds The Brotherton Library, Wiley Online Library on [28/05/2026]. See the Terms and Conditions (https://onlinelibrary.wiley.com/terms-and-conditions) on Wiley Online Library for rules of use; OA articles are governed by the applicable Creative Commons License

behavior exhibited by H22, something E_c, which is based on particle size, fails to do. This highlights a limitation of E_c when applied beyond a size threshold where cohesion effects start to appear. Given that the scatter in the data using E_τ is within an acceptable range, as discussed, the erosion behavior of both cohesionless systems and those where cohesional forces start to operate can be reasonably modeled effectively based on their yield behavior alone using E_τ.

4 | CONCLUSIONS

This study investigated the erosion behavior of beds of Honite soda lime glass particles under impinging jet conditions, focusing on the role of particle size. An ultrasonic velocity profiler was employed to measure crater profiles, revealing significant impacts of particle size on erosion and crater profiles. For finer particles, the jet effectively eroded material near the jet centerline, while larger particles were trapped in the recirculation zone and resettled within the crater. As expected from cohesionless erosion, smaller particles produced larger crater profiles with smaller ring peaks. However, the smallest particles ($d_{50} = 35$ μm) exhibited no peaks and did not form the largest craters, indicating the onset of cohesive effects at this particle size.

This transition to cohesion was further supported by the increase in yield stress for the smallest particles, contrasting with the general trend where yield stress decreases with decreasing particle size. Additionally, when modeled using the erosion parameter E_c, the data for the smallest particle size deviated from other Honite particle data. It was found that E_c remains effective for modeling cohesionless particles down to a certain size limit, beyond which cohesive forces become significant and the relationship changes. On the other hand, a new parameter (E_τ) was defined based on the critical shear stress of the bed (measured through the shear yield stress) and derived from a force balance at the crater interface. Using this shear-yield erosion parameter, the transition to cohesion was accounted for when fitting the erosion across the whole of the particle range, where the smallest particles aligned well with the other glass data. Overall, this work provides important evidence into the transition point of cohesive-cohesionless systems for well dispersed spherical particles undergoing erosion, where modeling based on the sediment yield stress was found to be an innovative and straightforward approach to predicting all systems.

AUTHOR CONTRIBUTIONS

Ahmad Mohamadiyeh: Writing—original draft; investigation; methodology; validation; software; formal analysis, and data curation. **Jeffrey Peakall**: Writing—review and editing; supervision; resources, and conceptualization. **Michael Fairweather**: Conceptualization; writing—review and editing; supervision, and project administration. **Martyn Barnes**: Writing—review and editing; supervision; project administration; funding acquisition, and conceptualization. **Timothy N. Hunter**: Writing—review and editing; supervision; resources; project administration; methodology, and conceptualization.

ACKNOWLEDGMENTS

This work was supported by the Engineering and Physical Research Council (EPSRC) UK, and Sellafield Ltd., through the EPSRC Center for Doctoral Training in Future Fluid Dynamics (Grant number: EP/S022732/1). We would like to thank Dr. Gareth Keevil and Helena Brown from the Sorby Laboratory for providing, and assistance with, the UVP. Special thanks are given to Dr. Alastair Baker with further support from the EPSRC MULTI-Form National Nuclear Users Facility (Grant number: EP/V034898/1) for funding and access to the high-resolution traverse. We are also grateful to Robert Harris for constructing the UVP holder and the UVP-traverse arm and Diane Cochrane for providing and organizing the laboratory space. Our appreciation extends to Dr. Ben Douglas for his technical assistance with the Mastersizer and SEM. Finally, we thank Chris Bulman for providing laboratory technical support. Lastly, thanks are given to the anonymous reviewer and the editor for their valuable feedback, which improved the manuscript.

CONFLICT OF INTEREST STATEMENT

The authors declare no conflicts of interest.

DATA AVAILABILITY STATEMENT

The data that support the findings of this study are openly available in University of Leeds Data Repository at https://doi.org/10.5518/1730.

ORCID

Ahmad Mohamadiyeh https://orcid.org/0009-0000-8379-5328
Michael Fairweather https://orcid.org/0000-0001-7568-2235

REFERENCES

1. Guguloth S, Pandey M. A review of literature on the scour process under different jets conditions. *J Irrig Drain Eng*. 2023;149(10):04023022.
2. Al-Madhhachi A, Hanson G, Fox G, Tyagi A, Bulut R. Measuring erodibility of cohesive soils using laboratory jet erosion tests. Paper presented at: World Environmental and Water Resources Congress 2011: Bearing Knowledge for Sustainability. 2011.
3. Wahl TL. The submerged jet erosion test: past-present-future. Paper presented at: Proc., USSD Int. Symp. On the Mechanics of Internal Erosion for Dams and Levees, Westminster. United States Society on Dams. 2016.
4. Metzger PT. Erosion rate of lunar soil under a landing rocket, part 1: identifying the rate-limiting physics. *Icarus*. 2024;417:116136.
5. Bamberger JA, Pease LF, Minette MJ. Solids erosion patterns developed by pulse jet mixers. Paper presented at: Fluids Engineering Division Summer Meeting. 2017.
6. Pease LF, Bamberger JA, Minette MJ. Jet erosion of particle beds: projecting critical suspension velocities from effective clearing/cleaning radii. Paper presented at: Fluids Engineering Division Summer Meeting. 2022.
7. Bux J, Paul N, Hunter TN, Peakall J, Dodds JM, Biggs S. *In situ* characterization of mixing and sedimentation dynamics in an impinging jet ballast tank via acoustic backscatter. *AIChE J*. 2017;63(7):2618-2629.
8. McArthur GA, Tinsley TP, McKendrick D. Development of a liquid jet sludge re-suspension model: (used on pulse jets or jet ballasts). Paper presented at: AIChE Annual Meeting 2005; Cincinnati, OH. 2005.

15475905, 2026, 6, Downloaded from https://aiche.onlinelibrary.wiley.com/doi/10.1002/aic.70336 by University Of Leeds The Brotherton Library, Wiley Online Library on [28/05/2026]. See the Terms and Conditions (https://onlinelibrary.wiley.com/terms-and-conditions) on Wiley Online Library for rules of use; OA articles are governed by the applicable Creative Commons License

9. Rahman H, Hunter T, Heggs P. Simplified heat transfer model for highly active raffinate contained in buffer storage tanks. *Chem Eng Res Des*. 2023;190:464-475.
10. Lick W, Jin L, Gailani J. Initiation of movement of quartz particles. *J Hydraul Eng*. 2004;130(8):755-761.
11. Zou R, Gan M, Yu A. Prediction of the porosity of multi-component mixtures of cohesive and non-cohesive particles. *Chem Eng Sci*. 2011; 66(20):4711-4721.
12. Roberts J, Jepsen R, Gotthard D, Lick W. Effects of particle size and bulk density on erosion of quartz particles. *J Hydraul Eng*. 1998; 124(12):1261-1267.
13. Righetti M, Lucarelli C. May the Shields theory be extended to cohesive and adhesive benthic sediments? *J Geophys Res Oceans*. 2007; 112(C5):C05039.
14. Beltaos S, Rajaratnam N. Impinging circular turbulent jets. *J Hydraul Div*. 1974;100(10):1313-1328.
15. Abramovich GN, Girshovich T, Krasheninnikov SI, Sekundov A, Smirnova I. *The Theory of Turbulent Jets*. MIT Press; 1984.
16. Aderibigbe O, Rajaratnam N. Erosion of loose beds by submerged circular impinging vertical turbulent jets. *J Hydraul Res*. 1996;34(1): 19-33.
17. Chakravarti A, Jain R, Kothyari U. Scour under submerged circular vertical jets in cohesionless sediments. *ISH J Hydraul Eng*. 2014;20(1): 32-37.
18. Hunter TN, Peakall J, Unsworth TJ, et al. The influence of system scale on impinging jet sediment erosion: observed using novel and standard measurement techniques. *Chem Eng Res Des*. 2013;91(4): 722-734.
19. Chen J, Zhang G, Si J-H, Shi H, Wang X. Experimental investigation of scour of sand beds by submerged circular vertical turbulent jets. *Ocean Eng*. 2022;257:111625.
20. Palermo M, Di Nardi J, Bombardelli FA, Pagliara S. Scour due to circular jets in cohesive soils: physical evidence from three-dimensional laboratory tests. *Phys Fluids*. 2024;36(9):095169.
21. Hamm B, West W, Tatterson GB. Sludge suspension in waste storage tanks. *AIChE J*. 1989;35(8):1391-1394.
22. Mazurek K, Rajaratnam N, Sego D. Scour of cohesive soil by submerged circular turbulent impinging jets. *J Hydraul Eng*. 2001;127(7): 598-606.
23. Brunier-Coulin F, Cuéllar P, Philippe P. Generalized Shields criterion for weakly cohesive granular materials. *Phys Rev Fluids*. 2020;5(3): 034308.
24. Bombardelli FA, Palermo M, Pagliara S. Temporal evolution of jet induced scour depth in cohesionless granular beds and the phenomenological theory of turbulence. *Phys Fluids*. 2018;30(8):085109.
25. Brunier-Coulin F, Cuéllar P, Philippe P. Erosion onset of a cohesionless granular medium by an immersed impinging round jet. *Phys Rev Fluids*. 2017;2(3):034302.
26. Kartal V, Emiroglu ME. Effect of nozzle type on local scour in water jets: an experimental study. *Ocean Eng*. 2023;277:114323.
27. Baldi M, Mendina M, Chreties C. Experimental and numerical study of sediment scour under impinging vertical jet. Paper presented at: International Conference on Computational Heat and Mass Transfer; Switzerland. 2023.
28. Maiti R, Shepley P. Penetration of jet piles on submerged granular beds. *Ocean Eng*. 2025;315:119914.
29. Guleria SD, Patil DV. Experimental investigations of crater formation on granular bed subjected to an air-jet impingement. *Phys Fluids*. 2020;32(5):053309.
30. LaMarche CQ, Curtis JS. Cratering of a particle bed by a subsonic turbulent jet: effect of particle shape, size and density. *Chem Eng Sci*. 2015;138:432-445.
31. Badr S, Gauthier G, Gondret P. Crater jet morphology. *Phys Fluids*. 2016;28(3):033305.
32. Dunnett B, Ward T, Roberts R, Cheesewright J. Physical properties of highly active liquor containing molybdate solids. *Proc Chem*. 2016;21: 24-31.
33. Guyson. *Blast Media Data Sheet*, Guyson International Limited; 2024. Accessed 2024. https://s3-eu-west-1.amazonaws.com/resources.guyson.co.uk/product-downloads/Honite.pdf?mtime=20250131122835
34. Allen T. *Particle Size Measurement*. Springer; 2013.
35. Merkus HG. *Particle Size Measurements: Fundamentals, Practice, Quality*. Vol 17. Springer Science & Business Media; 2009.
36. Tonge AS, Peakall J, Cowell DM, Freear S, Barnes M, Hunter TN. Experimental validation of acoustic inversions for high concentration profiling of spherical particles, using broadband technology in the Rayleigh regime. *Appl Acoust*. 2021;180:108100.
37. Dzuy NQ, Boger DV. Yield stress measurement for concentrated suspensions. *J Rheol*. 1983;27(4):321-349.
38. Dzuy NQ, Boger DV. Direct yield stress measurement with the vane method. *J Rheol*. 1985;29(3):335-347.
39. Dullien FA. *Porous Media: Fluid Transport and Pore Structure*. Academic Press; 2012.
40. Shukla AK, Dewan A. Flow and thermal characteristics of jet impingement: comprehensive review. *Int J Heat Technol*. 2017;35(1):153-166.
41. Mao J, Si J-H, Li G, Zhou B, Wang X. Self-similarity of sand bed scour by an oblique impinging plane jet under different Reynolds numbers. *Ocean Eng*. 2023;288:116037.
42. Schneider CA, Rasband WS, Eliceiri KW. NIH Image to ImageJ: 25 years of image analysis. *Nat Methods*. 2012;9(7):671-675.
43. Luetzenburg G, Kroon A, Bjørk AA. Evaluation of the Apple iPhone 12 pro LiDAR for an application in geosciences. *Sci Rep*. 2021;11(1):1-9.
44. Monsalve A, Yager EM, Tonina D. Evaluating Apple iPhone LiDAR measurements of topography and roughness elements in coarse bedded streams. *J Ecohydraul*. 2023;10:1-11.
45. Thorne PD, Hanes DM. A review of acoustic measurement of small-scale sediment processes. *Cont Shelf Res*. 2002;22(4):603-632.
46. Higashi N, Sumita I. Experiments on granular rheology: effects of particle size and fluid viscosity. *J Geophys Res Solid Earth*. 2009;114(B4): B04212.
47. Chen D, Wang Y, Melville B, Huang H, Zhang W. Unified formula for critical shear stress for erosion of sand, mud, and sand–mud mixtures. *J Hydraul Eng*. 2018;144(8):04018046.
48. Zhou Z, Solomon MJ, Scales PJ, Boger DV. The yield stress of concentrated flocculated suspensions of size distributed particles. *J Rheol*. 1999;43(3):651-671.
49. Louati H, Oulahna D, de Ryck A. Effect of the particle size and the liquid content on the shear behaviour of wet granular material. *Powder Technol*. 2017;315:398-409.
50. Hao S, Rahul M, Somik C, Ramon C, Martin M, Harald Z. Effect of particle size and cohesion on powder yielding and flow. *KONA Powder Particle J*. 2018;35:226-250.
51. Johnson M, Fairweather M, Harbottle D, Hunter TN, Peakall J, Biggs S. Yield stress dependency on the evolution of bubble populations generated in consolidated soft sediments. *AIChE J*. 2017;63(9): 3728-3742.
52. Barnes HA, Nguyen QD. Rotating vane rheometry—a review. *J Non-Newtonian Fluid Mech*. 2001;98(1):1-14.
53. Daniel RC, Poloski AP, Saez AE. Vane rheology of cohesionless glass beads. *Powder Technol*. 2008;181(3):237-248.
54. Shields A. *Application of Similarity Principles and Turbulence Research to Bed-Load Movement*, California Institute of Technology; 1936.
55. Cao Z, Pender G, Meng J. Explicit formulation of the Shields diagram for incipient motion of sediment. *J Hydraul Eng*. 2006;132(10):1097-1099.
56. Coleman S, Nikora V. A unifying framework for particle entrainment. *Water Resour Res*. 2008;44(4):W04415.

15475905, 2026, 6, Downloaded from https://aiche.onlinelibrary.wiley.com/doi/10.1002/aic.70336 by University Of Leeds The Brotherton Library, Wiley Online Library on [28/05/2026]. See the Terms and Conditions (https://onlinelibrary.wiley.com/terms-and-conditions) on Wiley Online Library for rules of use; OA articles are governed by the applicable Creative Commons License

57. Chen K-l, Wei W-r, Deng J. Morphology evolution of three-dimensional scours under submerged jets. *Front Earth Sci*. 2022;10:917447.
58. Nazarimehr F, Ghodsian M. Experimental study of scour characteristics by circular turbulent impinging jets in cohesive soils. *ISH J Hydraul Eng*. 2025;31:2481936.
59. Rushton JH. The axial velocity of a submerged axially symmetrical fluid jet. *AIChE J*. 1980;26(6):1038-1041.
60. Mao J, Si J-H, Li G, Wang X. Comparison of flow characteristics of plane jet impingement on a solid plate and on a sand bed. *Phys Fluids*. 2024;36(3):035152.
61. Vessaire J, Varas G, Joubaud S, Volk R, Bourgoin M, Vidal V. Stability of a liquid jet impinging on confined saturated sand. *Phys Rev Lett*. 2020;124(22):224502.
62. Amin MM, Rajaratnam DN, Zhu D. Scour of sand beds by long and short impinging jets-similarities and differences. Paper presented at: Proceedings of the 39th IAHR World Congress. 2022.
63. Yeh P-H, Chang K-A, Henriksen J, et al. Large-scale laboratory experiment on erosion of sand beds by moving circular vertical jets. *Ocean Eng*. 2009;36(3–4):248-255.
64. Amin MR, Rajaratnam N, Zhu DZ. Scouring of sand beds by short impinging turbulent jets. *Proceedings of the Institution of Civil Engineers—Water Management*. Vol 174. Thomas Telford Ltd; 2021:309-320.
65. Mazurek KA, Hossain T. Scour by jets in cohesionless and cohesive soils. *Can J Civ Eng*. 2007;34(6):744-751.
66. Sharma RS, Gong M, Azadi S, Gans A, Gondret P, Sauret A. Erosion of cohesive grains by an impinging turbulent jet. *Phys Rev Fluids*. 2022;7(7):074303.
67. Rajaratnam N. *Turbulent Jets*. Elsevier; 1976.

SUPPORTING INFORMATION

Additional supporting information can be found online in the Supporting Information section at the end of this article.

How to cite this article: Mohamadiyeh A, Peakall J, Fairweather M, Barnes M, Hunter TN. Erosion of granular sediments by submerged impinging jets: Particle size effects and cohesion onset. *AIChE J*. 2026;72(6):e70336. doi:10.1002/aic.70336

15475905, 2026, 6, Downloaded from https://aiche.onlinelibrary.wiley.com/doi/10.1002/aic.70336 by University Of Leeds The Brotherton Library, Wiley Online Library on [28/05/2026]. See the Terms and Conditions (https://onlinelibrary.wiley.com/terms-and-conditions) on Wiley Online Library for rules of use; OA articles are governed by the applicable Creative Commons License